Frequency multiplication by collective nano-scale spin wave dynamics

Georg Woltersdorf (georg.woltersdorf@physik.uni-halle.de)
Martin Luther University Halle-Wittenberg
Rouven Dreyer
Martin Luther University Halle-Wittenberg
Niklas Liebing
Martin Luther University Halle-Wittenberg
Chris Körner
Martin Luther University Halle-Wittenberg
Martin Wagener
ETH Zuerich

Physical Sciences - Article

Keywords: spin wave dynamics, frequency multiplication, magnetism

Posted Date: June 4th, 2021

DOI: https://doi.org/10.21203/rs.3.rs-577652/v1

Frequency multiplication by collective nanoscale spin wave dynamics

Chris Körner[1], Rouven Dreyer[1], Martin Wagener[2], Niklas Liebing[1], and Georg Woltersdorf[1,*]

[1]Institute of Physics, Martin Luther University Halle-Wittenberg, Von-Danckelmann-Platz 3, 06120 Halle, Germany
[2]Department of Physics, ETH Zürich, 8093 Zürich, Switzerland
[*]Corresponding author: Georg Woltersdorf, georg.woltersdorf@physik.uni-halle.de

May 31, 2021

Abstract

Frequency multiplication is a process where harmonic multiples of the input frequency are generated. It is usually achieved in non-linear electronic circuits [1] or transmission lines [2]. Such elements enable the up-conversion of electronic signals to GHz frequencies and are essential for frequency synthesizers and communication devices. Circuits based on the propagation and interaction of spin waves are a promising alternative to conventional electronics [3, 4]. Unfortunately, these systems usually require direct driving in the GHz range as magnonic frequency up-conversion is restricted to a few harmonics only [5–7]. Here we show that the ferromagnetic material itself can act as a six octave spanning frequency multiplier. By studying low frequency magnetic excitations in a continuous ferromagnetic layer we show that the non-linearity of magnetization dynamics combined with disorder in the ferromagnet leads to the emergence of a dynamic phase generating high harmonics. The demonstrated broad band frequency multiplication opens exciting perspectives for magnonic and spintronic applications since the frequency is up-converted from MHz into GHz frequencies within the magnetic medium itself. Due to the ease at which magnetic media can be structured and modified spatially (and reversibly) we anticipate that a tailored non-linear dynamic phase can be engineered e.g. to stabilize magnetic solitons [8–10].

Spin waves in magnetic materials typically oscillate in the GHz range. For many applications the possibility of frequency up-conversion using the non-linearity of the magnetization dynamics would be desirable but has been restricted typically to a few harmonics only [5–7]. Such non-perturbative frequency multiplication processes over several octaves were only observed at optical frequencies in response to extremely intense laser pulses [11, 12]. The non-linear behavior can either emerge when an external driving force exceeds a threshold or from the intrinsic non-linearity of the equation of motion itself. In the case of spin waves major attention went into studying the threshold behavior with respect to the radio frequency (rf) pumping field showing that large excitation amplitudes drive non-linear spin wave modes [13–17]. These non-linear excitations are utilized in spintronic devices such

as memory applications [18–21] and spin transfer torque-driven nano-oscillators [22–26]. As the stiffness is reduced in a magnetic system, highly elliptical precession at high amplitudes can be excited. In this regime the motion of the magnetization vector itself generates a large modulation field acting back on the magnetization rendering the Suhl instability model [13] invalid. For large modulation amplitudes critical spin waves emerge at half integer multiples of the pumping frequency [27].

In this article, we explore the non-linear response of a soft ferromagnet close to zero magnetic field at large driving amplitudes and small frequencies. Spin waves are probed using diamond Nitrogen vacancy (NV) center nanoscale magnetometry [28–34] and time-resolved magneto optic Kerr microscopy (MOKE) [35–37]. In the measurements we indeed find evidence for the expected spin waves precessing at 3/2 of the driving frequency and - very surprisingly - a series of additional spin wave excitations precessing at up to the 60^{th} harmonic of the pumping frequency. This result can be understood by a generalized theory of spin-wave turbulence.

In experiments a ferromagnetic (FM) $Ni_{80}Fe_{20}$ layer is deposited on top of an Au coplanar waveguide (CPW) and covered with nano-diamonds containing NV centers [28, 29, 33, 38], as illustrated in Fig. 1a. The rf magnetic fields generated by the CPW excite the electron spin resonance (ESR) in diamond NV centers as well as magnetization dynamics in the FM layer. In NV center magnetometry the ESR of the NV centers is optically detected by monitoring their photoluminescence (PL), i.e., optical detection of magnetic resonance (ODMR) [39–41]. Fig. 1b shows the measured PL intensity modulation due to microwave excitation recorded from the NV center ensemble as a function of static bias field and the rf excitation frequency, f_{rf}.

Whenever applied magnetic field and rf frequency coincide with the ESR condition an increase in the PL signal is observed. In addition to the expected ESR signal of the individual NV centers (dotted lines in Fig. 1b), we find a number of additional features in the ODMR signal due to the proximity of the FM layer. At first glance these may be characterized as follows: (I) a continuous resonance at and below the ferromagnetic resonance (FMR) field, (II) a strong enhancement at 2/3 of the NV centers resonance frequency and (III) a series of resonance lines at low bias fields. The occurrence of the FMR in the ODMR signal (I) has been observed before [30–33, 42, 43] and the effect is attributed to dipolar stray fields generated by spin waves acting on the NV centers [31]. Feature (II) occurs

at a frequency of 2/3 f_{ESR}, i.e., at $1.9\,\mathrm{GHz}$. The observation of resonance at a fractional multiple of the ESR frequency is at a first glance not expected. However, recently indirect evidence of non-linear spin wave generation at 3/2 f_{rf} has been reported for small bias fields [27]. The corresponding dynamic stray fields lead to an ODMR signal if the driving frequency matches 2/3 f_{ESR} confirmed by the experiment. Furthermore, in agreement with the prediction these spin wave modes follow a threshold behavior, as shown in extended data Fig. S2.

For magnetic fields below $4\,\mathrm{mT}$ a series of narrow resonance lines whose spacing scales down with decreasing frequency as shown in Fig. 2 is observed (feature III). One finds that these lines actually represent a frequency comb and occur at frequencies f_{ESR}/n, where n is an integer. In fact, all of these resonances are very sharp replicas of the ESR cone of the NV centers (around $2.87\,\mathrm{GHz}$) occurring at n^{th} fraction of the ESR frequency. The observed Zeeman splitting of the harmonic resonances is proportional to the bias field and scales inversely with the mode number n. In the inset of Fig. 2 more than 60 harmonics of the excitation frequency are observed with a signal amplitude comparable to the main ESR signal of the NV ensemble and only weakly decaying with increasing n. The harmonic ESR lines are a consequence of the presence of the FM layer (see extended data Figure S1 for more details) and their origin must be attributed to the dynamic response of the FM layer. The observation of such a frequency comb is not at all expected and deserves close attention.

In order to investigate the spin wave modes responsible for the frequency comb we directly map the dynamic response at higher harmonics of the excitation using super-Nyquist-sampling MOKE (SNS-MOKE). We observe a frequency comb of the fundamental frequency (in this case $191\,\mathrm{MHz}$) which surprisingly extends up to several GHz. In this particular case, the 15$^{\mathrm{th}}$ harmonic of the generated frequency comb matches the ESR ($15 \cdot 191\,\mathrm{MHz} = 2.87\,\mathrm{GHz}$) frequency and thereby causes the ODMR signal observed at $191\,\mathrm{MHz}$ f_{rf}. The same argument applies for all sub-harmonic frequencies f_n whenever $n \cdot f = 2.87\,\mathrm{GHz}$ is satisfied resulting in the frequency comb. In Fig. 3 spatially-resolved measurements of magnitude and phase of the dynamic magnetization are shown exemplary of the 1$^{\mathrm{st}}$, 10$^{\mathrm{th}}$, and 20$^{\mathrm{th}}$ harmonic. Here one finds an almost homogeneous response at the first harmonic (fundamental) and an increasingly fragmented spatial modulation in the micron and sub-micron range for higher harmonics (all harmonics in extended data Fig. S5). The frequency comb generation is most

pronounced at magnetic bias fields below $2\,\mathrm{mT}$.

We perform micromagnetic simulations in order to understand this peculiar behavior. Interestingly, a simulation of a homogeneous magnetic layer cannot reproduce the observed behavior as the experimental result differs in two important points: First, only a few harmonics of the excitation frequency are predicted, as shown for $f_{\mathrm{rf}} = 191\,\mathrm{MHz}$ in Fig. 4a (red curve). Second, the simulation only predicts odd harmonics in the z component of the stray field. This result is not surprising since, based on the equation of motion of the magnetization and its intrinsic non-linearity, one indeed expects just a few odd harmonics with rapidly decreasing amplitude. However, the experiment does not show any difference between even and odd harmonics. Therefore, a crucial aspect must be missing in the discussion.

Given an excitation amplitude of a few hundred $\mu\mathrm{T}$ and the magnetic bias field (stiffness) of similar magnitude one can expect large in-plane excursion angles for the magnetization of up to $45\,\mathrm{deg}$. In this case, the typical description of non-linear magnetization dynamics via first and second order Suhl instabilities [13] becomes invalid. Here, a description which takes the large modulation amplitude into account is required. To this end, we consider a solution of the equation of motion directly in k-space. The Landau-Lifshitz-Gilbert (LLG) equation is transformed to the Mathieu equation [44] and real and imaginary parts of the spin-wave frequency are numerically evaluated as function of the in-plane wave vector [27]. This approach ensures a valid description of magnetization dynamics even in the limit of strong modulation. Figures 4b and 4c depict the results of this treatment. The equation of motion alone in the case of strong driving gives rise to strongly increased spin-wave lifetimes at discrete points in k-space. These lifetime pockets allow for the existence of previously unexpected exotic spin wave modes at multiples of the excitation frequency. However, this important finding alone does not explain why it is even possible to populate these modes.

So far, we only considered the idealized case of uniform magnetization. However, it is known that soft magnetic materials such as $Ni_{80}Fe_{20}$ can exhibit a non-collinear spin texture at very low internal magnetic fields e.g., due to a spatially varying anisotropy or dipolar effects induced by roughness or polycrystallinity. At low magnetic fields this effect typically results in a broad magnetic resonance response [45] as well as so called concertina patterns [46]. Intuitively, one can now see how non-

collinearity may promote the observed harmonic generation in presence of a uniform driving field: the increased lifetimes arising from the strong modulation in the equation of motion in combination with the non-uniformity of the magnetic texture provides the momentum necessary for direct excitation into those modes and facilitates the observed mutual frequency multiplication. This reasoning is confirmed by including a small variation of the magnetic properties into the micromagnetic simulation. As shown in Fig. 4a (blue curve) a small inhomogeneity results in a dramatic change, i.e. an emerging frequency comb extending up to $4\,\mathrm{GHz}$, consistent with our experimental findings.

Our results demonstrate that all the - at first glance very surprising - phenomena in the PL signal can be explained by the rather peculiar dynamic behavior of the ferromagnetic layer. Very interestingly, a simple and nominally homogeneous layer of ferromagnetic material (in our case $Ni_{80}Fe_{20}$) can be used to generate a frequency comb spanning 6 octaves. Using time-resolved Kerr microscopy we can correlate this frequency multiplying behavior to the emergence of a collective dynamic phase. As we demonstrate by the magneto optic images (Fig. 3) a standing spin wave pattern establishes itself at all harmonics of the excitation frequency within the spin wave band. The wave vector of the excited spin wave patterns roughly follows the center of the corresponding spin wave band as illustrated in extended data Fig. S6. Interestingly, a certain amount of disorder in the magnetization is required in the simulations in order to reproduce the experimental result.

From a fundamental point of view the effect of phase stable pattern formation at many harmonics discussed in this article represents a self synchronization phenomenon. Such effects are occurring in a large variety of systems ranging from the synchronization of planetary or moon orbits [47], periodic chemical reactions [48] to crowd synchronization in behavioral analytics [49]. In the present case the rf excitation at low bias field leads to the formation of a phase-stable time-periodic magnetization pattern and thus essentially realizes a driven Floquet system.

The presented possibility of frequency multiplication under cw conditions within the magnetic medium itself opens exciting perspectives for magnonic and spintronic applications operating in the GHz range while conveniently being controlled with MHz input signals. In future experiments, the properties of magnetic layers can be easily tuned by lithographic patterning or reversibly imprinting a magnetic texture via the application of magnetic fields or spin currents [50–52]. This paves the

way towards targeted engineering of all-magnetic devices utilizing the observed robust self-organized dynamic state e.g as spin wave sources, amplifiers or mixers as pure spin electronic devices. Furthermore, the observed phase-locked dynamics at the harmonics indicates the possibility to generate and stabilize magnetic solitons [8–10].

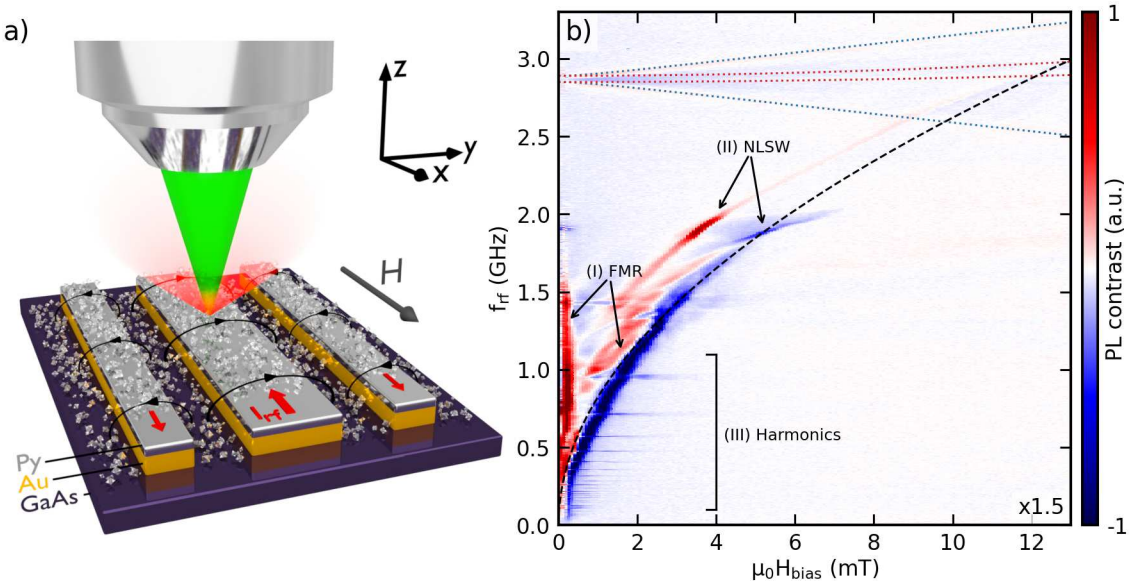

Fig. 1 | NV center detection of spin waves a) Measurement geometry. We investigate a $20\,\mathrm{nm}$ thick ferromagnetic $Ni_{80}Fe_{20}$ layer on top of a coplanar waveguide (CPW) by means of nano-diamonds containing NV centers dispersed on the sample, which act as local stray field sensors. b) Photoluminescence (PL) contrast as a function of bias field and excitation frequency. Blue and red dotted lines indicate the calculated electron spin resonance (ESR) of the NV centers. The adjacent ferromagnet introduces additional PL signals: (I) FMR, (II) non-linear spin waves at 2/3 of f_{ESR} and (III) a series of replicas of the ESR at low magnetic bias fields and frequencies.

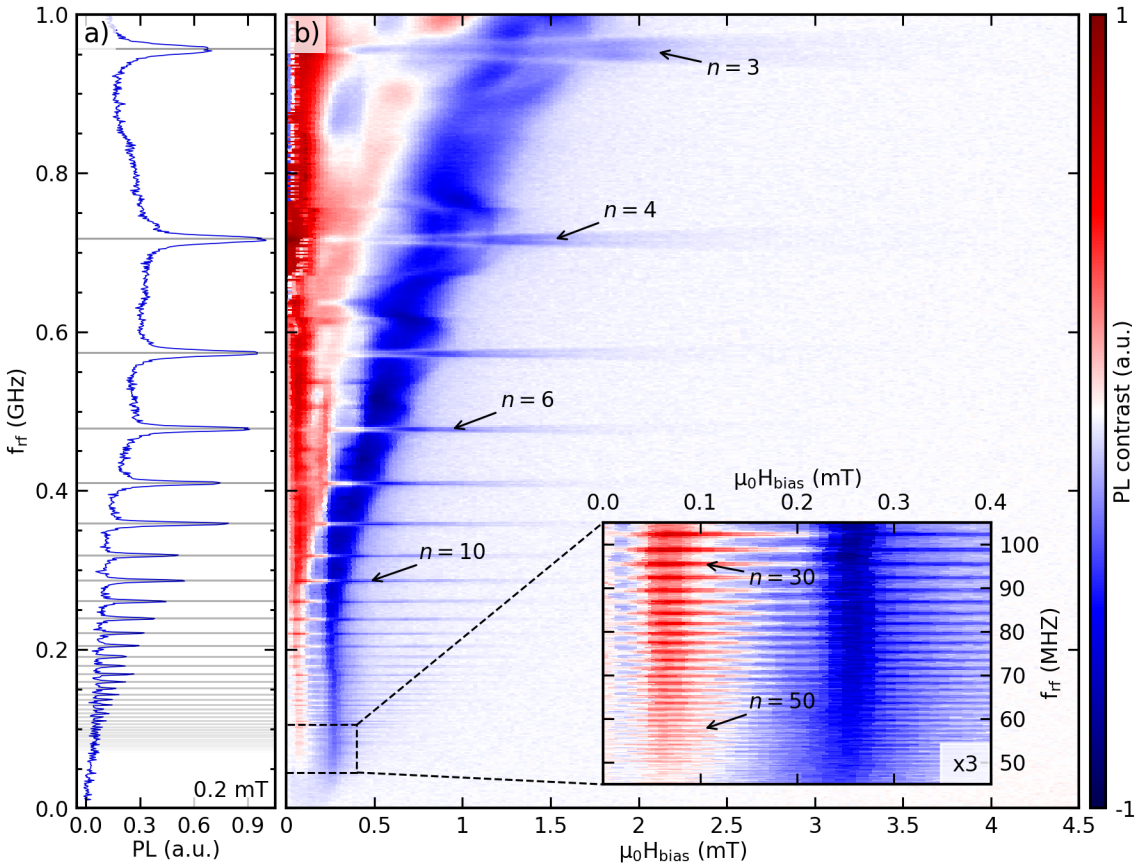

Fig. 2 | ODMR detection of frequency comb generation at low magnetic bias field. More than 50 harmonics of the driving frequency are detected (inset). The driving rf power is $16\,\mathrm{dBm}$. The left figure shows a cut at a constant bias field of $0.5\,\mathrm{mT}$ obtained with a different modulation method to suppress the FMR background (see Fig. S3 for a direct comparison). The grey lines indicate peak positions at $1/n$ fractions of the NV centers ESR frequency ($2.87\,\mathrm{GHz}$).

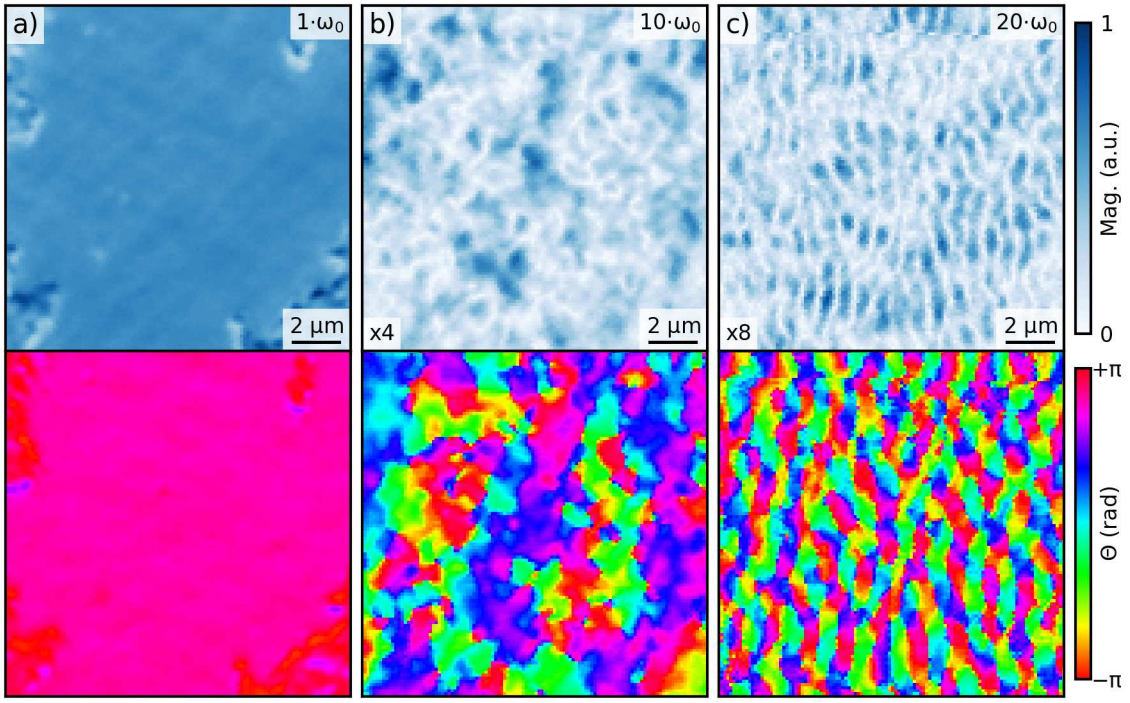

Fig. 3 | SNS-MOKE measurements. Spatially-resolved SNS-MOKE magnitude (upper panel) and phase (lower panel). All measurements were obtained at $0.5\,\mathrm{mT}$ bias field with a fixed excitation frequency of $191\,\mathrm{MHz}$ while the detection frequency was set to the a) 1^{st}, b) 10^{th} and c) 20^{th} harmonic of the excitation, respectively.

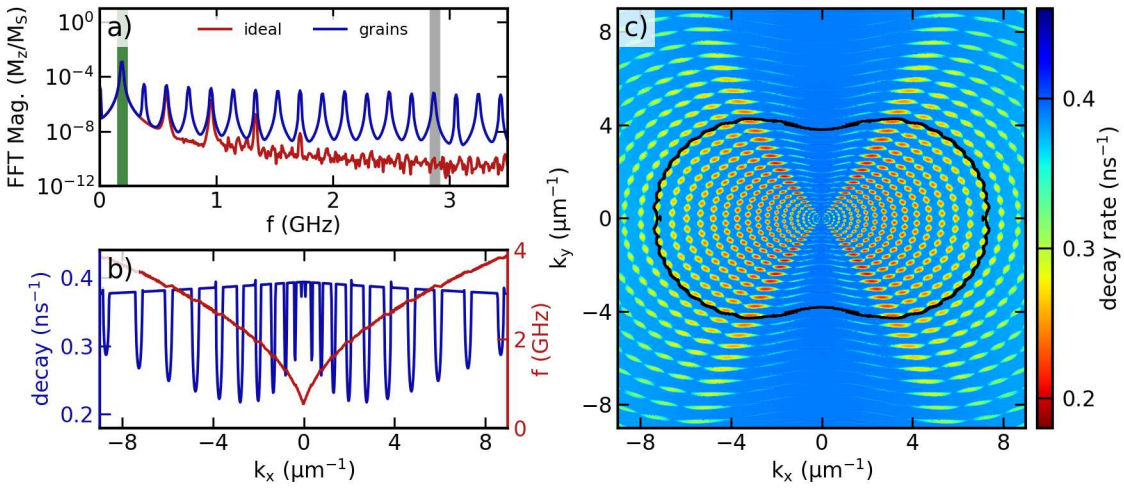

Fig. 4 | Micromagnetic simulation and k-space model. a) Fourier-Spectrum of the z-component of the magnetization simulated for an ideal and a more realistic film composed of grains having a slight variation of the magnetic properties. The simulations were carried out with a driving amplitude of $19\,\mathrm{dBm}$ at a frequency of $191\,\mathrm{MHz}$ (green area) and $0.5\,\mathrm{mT}$ bias field applied along x-axis. The grey area indicates the frequency f_{ESR} to which NV centers are sensitive. b) and c) show k-dependent decay rates in the spin wave spectrum obtained by solving the LLG equation in k-space. b) shows a cut at $\mathrm{k_y} = 0$. c) includes an examplary iso-frequency line (black) of the 11^{th} harmonic of the excitation frequency (here $319\,\mathrm{MHz}$).

Methods

Sample preparation

A CPW pattern was created on an MgO substrate via electron beam lithography (EBL). Subsequently, a layer sequence of $5\,\mathrm{nm}$ of Cr adhesive, $100\,\mathrm{nm}$ of Au and $20\,\mathrm{nm}$ of $Ni_{80}Fe_{20}$ was deposited on the sample via thermal deposition. After the lift-off, a $100\,\mathrm{nm}$-thick Al_2O_3 capping layer was deposited via atomic layer deposition (ALD). In a final step nano-diamonds are dispersed from a solution on top of the CPW. The sample was mounted on an rf-capable sample holder and the CPW was connected via wire bonds to the rf contacts.

ODMR setup

The ODMR setup consists of a confocal microscope where the sample is mounted on a three-axis piezo stage allowing for alignment or scanning the sample in spatially resolved measurements. An electromagnet is used to apply static bias fields of up to $150\,\mathrm{mT}$. The sample is illuminated with $532\,\mathrm{nm}$ cw laser light which is focused on the surface via a 0.6 NA objective. The $600\,\mathrm{nm}$ to $800\,\mathrm{nm}$ fluorescence light is collected with the objective and detected via an amplified photodiode. The fluorescence signal contains a proportion sensitive to rf excitation as well as magnetic field. Excitation powers of up to $22\,\mathrm{dBm}$ are realizable. The transmitted rf power through the sample is measured and used to calibrate the applied rf power over a large frequency range from $10\,\mathrm{MHz}$ up to $4\,\mathrm{GHz}$. To allow for lock-in detection of the PL signal, either the amplitude of the rf excitation applied through the CPW or the applied bias field can be modulated yielding different kinds of information (see extended data Fig. S3 for comparison).

Nano-diamonds

The nano-diamonds dispersed on top of the sample have an average size of $2\,\mathrm{nm}$ to $4\,\mathrm{nm}$ and contain one or a few NV centers each [38]. The thickness of the NV-center layer is estimated to a few $100\,\mathrm{nm}$ up to $1\,\mu\mathrm{m}$ as the nano-diamonds tend to stick together and form larger chunks. Because of the

dispersion procedure where the diamonds are taken from a solution the orientation of the individual diamonds lattice and therefore the orientation of the NV centers axes is randomly distributed with respect to the applied external bias field. Since every NV center experiences the projection of the bias field onto its axis, the effective field ranges from zero up to the full applied field. This causes the discrete Zeeman-split energy levels, which could be observed for a single NV center, to smear out and form a whole ESR-cone in case of the NV ensemble.

SNS-MOKE

In super-Nyquist sampling magneto-optical Kerr microscopy (SNS-MOKE) we utilize a femtosecond laser operating at $520\,\mathrm{nm}$ with a repetition rate of $80\,\mathrm{MHz}$. By exploiting aliasing processes SNS-MOKE allows to set the microwave excitation to arbitrary frequencies in contrast to conventional time-resolved techniques where the excitation is limited to discrete multiples of the repetition rate of the laser system. By overcoming this limitation and utilizing a multi-frequency lock-in amplifier simultaneous measurements at different harmonics of the driving frequency can be performed. Due to the inherent modulation scheme of the SNS-MOKE no external modulation (e.g., rf-amplitude modulation) is required and the obtained signals are proportional to the real and imaginary part of the dynamic susceptibility in the different harmonics.

Micromagnetic simulations

To corroborate the assumption that all of the observed features are caused by processes within the FM layer which is coupled to the NV ensemble in its vicinity via stray fields , micromagnetic simulations are carried out. For this purpose, the software package MuMax3 [53] is utilized to simulate the time evolution of the magnetization within the FM layer. The parameters of the model are based on the real sample properties. A $20\,\mathrm{nm}$ thick layer of FM with and without $100\,\mathrm{nm}$-sized grains to represent the polycrystalline properties of $Ni_{80}Fe_{20}$ is simulated. The magnetic parameters are $\alpha = 0.008$, $K_\mathrm{U} = 500\,\mathrm{J/m^3}$ and $M_\mathrm{Sat} = 866\,\mathrm{kA/m}$ which are expected for the $Ni_{80}Fe_{20}$ alloy used in the experiment. In grains are present, the parameters are randomly varied by up to $2\,\%$. During the simulation a static in-plane bias field is applied in x-direction along the CPW together with rf excitation perpendicular to

the CPW. The size of the simulated region is $5\,\mu\mathrm{m}$ by $5\,\mu\mathrm{m}$ with periodic boundary conditions making up for an infinitely sized sample. In this model we assume that the sample boundaries are irrelevant to reproduce the measured features. The simulated time trace of the magnetization is evaluated and by means of a fast Fourier transform (FFT) in each cell and subsequently averaged over the entire sample (Fig. 4).

Theoretical model

The processes observed in the experiments are mediated by the large elliptical precessional motion of the magnetization within the film plane. This ellipticity gives rise to an inherent frequency modulation within each precession period. To address this modulation, we utilized the model introduced by Bauer et al. [27] to directly solve the LLG equation in reciprocal space within the strong modulation regime. Therefore, the LLG equation is transformed into the Mathieu equation[44]

$$f'' + (a - 2q\cos(2x))f = 0 \tag{1}$$

where, $a = (\omega_\mathrm{k}/\omega_\mathrm{mod})^2$ contains the spin-wave frequency ω_k and the modulation frequency ω_mod and q is the modulation strength. The solution of the Mathieu equation has the form

$$F(a, q, x) = e^{i\nu(a,q)x} \cdot P(a, q, x) \tag{2}$$

with the complex Mathieu exponent $\nu(a, q)$ and a periodic function P. The real part of $\nu(a, q)$ for a given in-plane wave vector yields the frequency of the excited spin wave and thus results in the spin-wave dispersion as function of k_x and k_y. The imaginary part results in the spin-wave lifetime and allows to determine threshold values where non-linear spin waves become critical. The iso-frequency lines of higher harmonics and the corresponding increased spin-wave lifetimes were calculated by using the following parameters: $\alpha = 0.008$, $A_\mathrm{ex} = 13\,\mathrm{pJ/m}$ and $M_\mathrm{Sat} = 866\,\mathrm{kA/m}$.

References

1. Jian, Z. & Raeisaenen, A. *Survey on step recovery diode and its applications* NASA STI/Recon Technical Report N. 1994.

2. Salameh, D. & Linton, D. Microstrip GaAs nonlinear transmission-line (NLTL) harmonic and pulse generators. *IEEE Transactions on Microwave Theory and Techniques* **47,** 1118–1122 (1999).

3. Chumak, A. V., Vasyuchka, V. I., Serga, A. A. & Hillebrands, B. Magnon spintronics. *Nature Physics* **11,** 453–461 (2015).

4. Chumak, A. V., Serga, A. A. & Hillebrands, B. Magnonic crystals for data processing. *Journal of Physics D: Applied Physics* **50,** 244001 (2017).

5. Demidov, V. E. *et al.* Generation of the second harmonic by spin waves propagating in microscopic stripes. *Physical Review B* **83** (2011).

6. Rodrigues, D. R. *et al. Nonlinear dynamics of topological ferromagnetic textures for frequency multiplication* 2020. arXiv: `2012.11481 [cond-mat.mes-hall]`.

7. Hermsdoerfer, S. J. *et al.* A spin-wave frequency doubler by domain wall oscillation. *Applied Physics Letters* **94,** 223510 (2009).

8. Slavin, A. & Rojdestvenski, I. "Bright" and "dark" spin wave envelope solitons in magnetic films. *IEEE Transactions on Magnetics* **30,** 37–45 (1994).

9. Ustinov, A. B., Demidov, V. E., Kondrashov, A. V., Kalinikos, B. A. & Demokritov, S. O. Observation of the Chaotic Spin-Wave Soliton Trains in Magnetic Films. *Physical Review Letters* **106,** 017201 (2011).

10. Bonetti, S. *et al.* Direct observation and imaging of a spin-wave soliton with p-like symmetry. *Nature Communications* **6** (2015).

11. Schubert, O. *et al.* Sub-cycle control of terahertz high-harmonic generation by dynamical Bloch oscillations. *Nature Photonics* **8,** 119–123 (2014).

12. Popmintchev, T., Chen, M.-C., Arpin, P., Murnane, M. M. & Kapteyn, H. C. The attosecond nonlinear optics of bright coherent X-ray generation. *Nature Photonics* **4,** 822–832 (2010).

13. Suhl, H. The theory of ferromagnetic resonance at high signal powers. en. *Journal of Physics and Chemistry of Solids* **1,** 209–227 (1957).

14. Gerrits, T., Krivosik, P., Schneider, M. L., Patton, C. E. & Silva, T. J. Direct Detection of Nonlinear Ferromagnetic Resonance in Thin Films by the Magneto-Optical Kerr Effect. *Physical Review Letters* **98** (2007).

15. Olson, H. M., Krivosik, P., Srinivasan, K. & Patton, C. E. Ferromagnetic resonance saturation and second order Suhl spin wave instability processes in thin Permalloy films. *Journal of Applied Physics* **102,** 023904 (2007).

16. Schultheiss, H. *et al.* Direct Current Control of Three Magnon Scattering Processes in Spin-Valve Nanocontacts. *Physical Review Letters* **103** (2009).

17. Ulrichs, H., Demidov, V. E., Demokritov, S. O. & Urazhdin, S. Parametric excitation of eigenmodes in microscopic magnetic dots. *Physical Review B* **84,** 094401 (2011).

18. Daughton, J. M. Magnetic tunneling applied to memory (invited). *Journal of Applied Physics* **81,** 3758–3763 (1997).

19. Hu, J.-M., Li, Z., Chen, L.-Q. & Nan, C.-W. High-density magnetoresistive random access memory operating at ultralow voltage at room temperature. *Nature Communications* **2** (2011).

20. Zhu, J.-G., Zhu, X. & Tang, Y. Microwave Assisted Magnetic Recording. *IEEE Transactions on Magnetics* **44,** 125–131 (2008).

21. Okamoto, S., Kikuchi, N., Furuta, M., Kitakami, O. & Shimatsu, T. Microwave assisted magnetic recording technologies and related physics. *Journal of Physics D: Applied Physics* **48,** 353001 (2015).

22. Kaka, S. *et al.* Mutual phase-locking of microwave spin torque nano-oscillators. *Nature* **437,** 389–392 (2005).

23. Demidov, V. E. *et al.* Synchronization of spin Hall nano-oscillators to external microwave signals. *Nature Communications* **5** (2014).

24. Lebrun, R. *et al.* Mutual synchronization of spin torque nano-oscillators through a long-range and tunable electrical coupling scheme. *Nature Communications* **8** (2017).

25. Romera, M. *et al.* Vowel recognition with four coupled spin-torque nano-oscillators. *Nature* **563,** 230–234 (2018).

26. Haidar, M. *et al.* A single layer spin-orbit torque nano-oscillator. *Nature Communications* **10** (2019).

27. Bauer, H. G., Majchrak, P., Kachel, T., Back, C. H. & Woltersdorf, G. Nonlinear spin-wave excitations at low magnetic bias fields. en. *Nature Communications* **6** (2015).

28. Wolfe, C. S. *et al.* Off-resonant manipulation of spins in diamond via precessing magnetization of a proximal ferromagnet. en. *Physical Review B* **89** (2014).

29. Wolfe, C. S. *et al.* Spatially resolved detection of complex ferromagnetic dynamics using optically detected nitrogen-vacancy spins. *Applied Physics Letters* **108,** 232409 (2016).

30. Du, C. *et al.* Control and local measurement of the spin chemical potential in a magnetic insulator. en. *Science* **357,** 195–198 (2017).

31. Purser, C. M. *et al.* Spinwave detection by nitrogen-vacancy centers in diamond as a function of probe–sample separation. en. *Applied Physics Letters* **116,** 202401 (2020).

32. Lee-Wong, E. *et al.* Nanoscale Detection of Magnon Excitations with Variable Wavevectors Through a Quantum Spin Sensor. en. *Nano Letters* **20,** 3284–3290 (2020).

33. McCullian, B. A. *et al.* Broadband multi-magnon relaxometry using a quantum spin sensor for high frequency ferromagnetic dynamics sensing. *Nature Communications* **11,** 5229 (2020).

34. Bertelli, I. *et al.* Magnetic resonance imaging of spin-wave transport and interference in a magnetic insulator. *Science Advances* **6,** eabd3556 (2020).

35. Liensberger, L. *et al.* Spin-Wave Propagation in Metallic $Co_{25}Fe_{75}$ Films Determined by Microfocused Frequency-Resolved Magneto-Optic Kerr Effect. *IEEE Magnetics Letters* **10,** 1–5 (2019).

36. Trempler, P. *et al.* Integration and characterization of micron-sized YIG structures with very low Gilbert damping on arbitrary substrates. *Applied Physics Letters* **117,** 232401 (2020).

37. Qin, H. *et al.* Nanoscale magnonic Fabry-Pérot resonator for low-loss spin-wave manipulation. *Nature Communications* **12** (2021).

38. Schrand, A. M., Hens, S. A. C. & Shenderova, O. A. Nanodiamond Particles: Properties and Perspectives for Bioapplications. *Critical Reviews in Solid State and Materials Sciences* **34,** 18–74 (2009).

39. Balasubramanian, G. *et al.* Nanoscale imaging magnetometry with diamond spins under ambient conditions. *Nature* **455,** 648–651 (2008).

40. Schirhagl, R., Chang, K., Loretz, M. & Degen, C. L. Nitrogen-Vacancy Centers in Diamond: Nanoscale Sensors for Physics and Biology. en. *Annual Review of Physical Chemistry* **65,** 83–105 (2014).

41. Gross, I. *et al.* Real-space imaging of non-collinear antiferromagnetic order with a single-spin magnetometer. en. *Nature* **549,** 252–256 (2017).

42. Van der Sar, T., Casola, F., Walsworth, R. & Yacoby, A. Nanometre-scale probing of spin waves using single electron spins. *Nature Communications* **6,** 7886 (2015).

43. Page, M. R. *et al.* Optically detected ferromagnetic resonance in diverse ferromagnets via nitrogen vacancy centers in diamond. *Journal of Applied Physics* **126,** 124902 (2019).

44. Mathieu, É. Mémoire sur le mouvement vibratoire d'une membrane de forme elliptique. fre. *Journal de Mathématiques Pures et Appliquées* **13,** 137–203 (1868).

45. Nibarger, J. P., Lopusnik, R. & Silva, T. J. Damping as a function of pulsed field amplitude and bias field in thin film Permalloy. *Applied Physics Letters* **82,** 2112–2114 (2003).

46. Otto, F. & Steiner, J. The concertina pattern. *Calculus of Variations and Partial Differential Equations* **39,** 139–181 (2010).

47. Mills, S. M. *et al.* A resonant chain of four transiting, sub-Neptune planets. *Nature* **533,** 509–512 (2016).

48. Bray, C. A periodic reaction in homogeneous solution and it's relation to catalysis. *Contribution from the Chemical Laboratory of the University of California,* 6 (1921).

49. Strogatz, S., Abrams, D., McRobie, A., Eckhardt, B. & Edward, O. Crowd synchrony on the Millennium Bridge. *Nature* **438,** 43–44 (2005).

50. Chumak, A. V., Vasyuchka, V. I., Serga, A. A. & Hillebrands, B. Magnon spintronics. *Nature Physics* **11,** 453–461 (2015).

51. Demidov, V. E. *et al.* Excitation of coherent propagating spin waves by pure spin currents. *Nature Communications* **7** (2016).

52. Brächer, T., Pirro, P. & Hillebrands, B. Parallel pumping for magnon spintronics: Amplification and manipulation of magnon spin currents on the micron-scale. *Physics Reports* **699,** 1–34 (2017).

53. Vansteenkiste, A. *et al.* The design and verification of MuMax3. *AIP Advances* **4,** 107133 (2014).

Author contributions

G. W. conceived the study. C. K. and M. W. carried out the NV center experiments. R. D. carried out SNS-MOKE experiments. C. K. and N. L. fabricated the samples. N. L., C. K. and R. D. performed the simulations. All authors discussed and analyzed the results. G. W., C. K., R. D. and N. L. wrote the manuscript

Acknowledgements

We would like to acknowledge Dr. H. G. Bauer for providing the code for the k-space simulations. We would like to thank A. Schäffer for helpful discussions regarding micromagnetic simulations and Professor C. Degen for helpful discussions providing nano diamonds with NV centers. Financial support from the German research foundation (DFG) through Priority Program SPP 1538 (Spin Caloric Transport) and the European Research Council (ERC) via starting grant no. 280048 (ECOMAGICS) is gratefully acknowledged.

Competing interests

The authors declare no competing financial or non-financial interests.

Data availability

The data that support the findings of this study as well as the code employed are available from the corresponding author upon reasonable request.

Extended data and supplementary figures

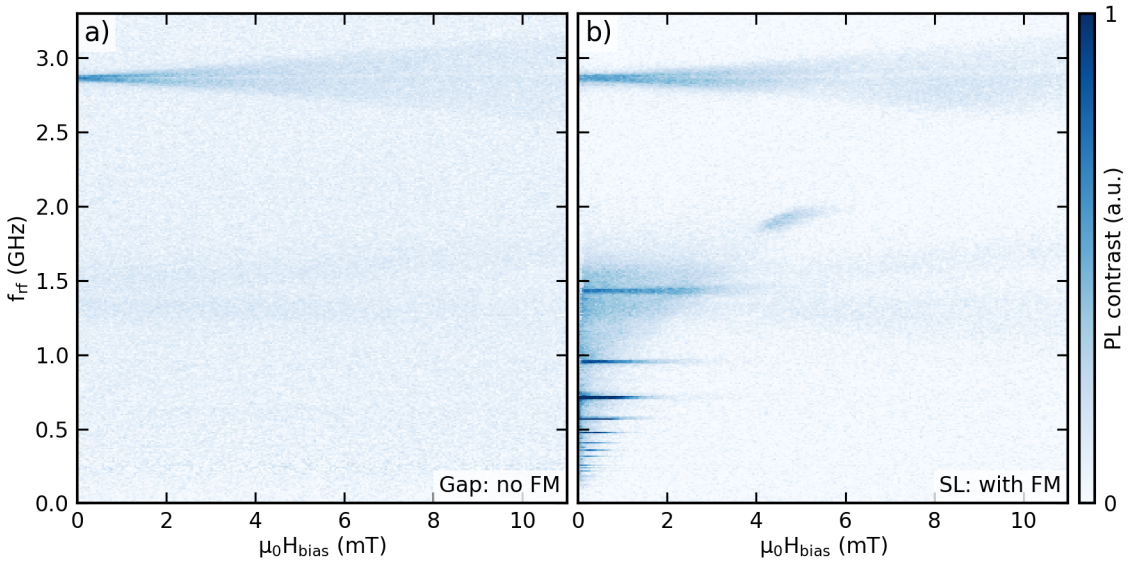

Fig. S1 | Influence of FM. Comparison of two measurements on the same sample, a) on the signal line (where the FM $Ni_{80}Fe_{20}$ is present) and b) in the gap of the CPW where it is not. Both measurements show the NV centers ESR at $2.87\,\mathrm{GHz}$, while only the FM measurement reveals plenty of different features at lower frequencies. The rf excitation power in both measurements is $16\,\mathrm{dBm}$ which results in slightly different driving amplitudes directly on the SL compared to the gap. To account for this the signals are scaled independently.

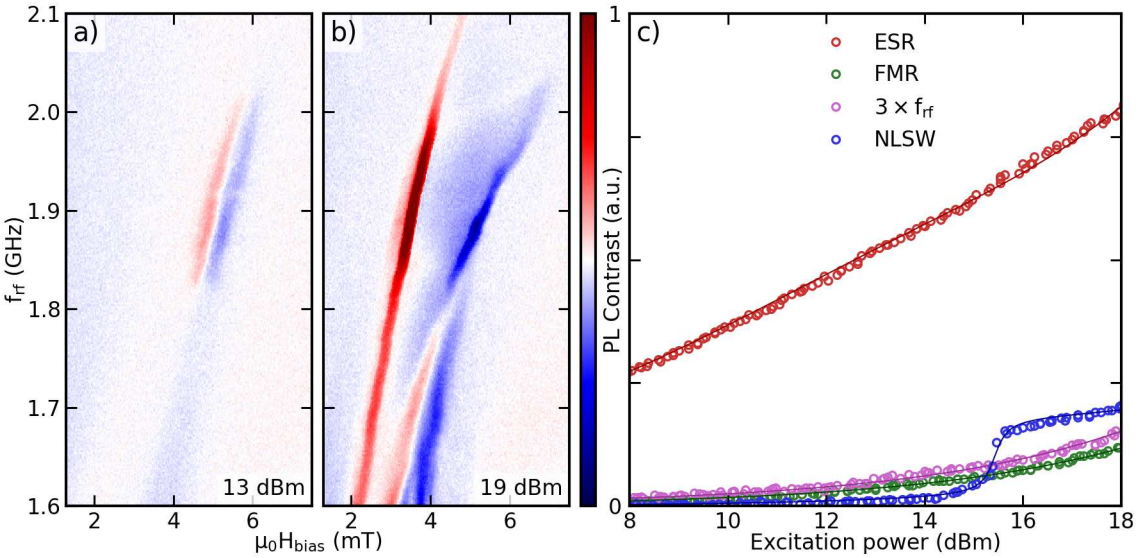

Fig. S2 | Power dependence of the PL signal. a,b) NLSW at 2/3 f_{ESR} exhibiting a threshold behavior, as expected for parametric spin wave generation. c) power dependence of the PL signal for ESR (2870 MHz, 1 mT), FMR (1200 MHz, 1.4 mT), 3rd harmonic (954 MHz, 2.3 mT) and NLSW (1940 MHz, 4.2 mT). The solid lines represent a guide to the eye.

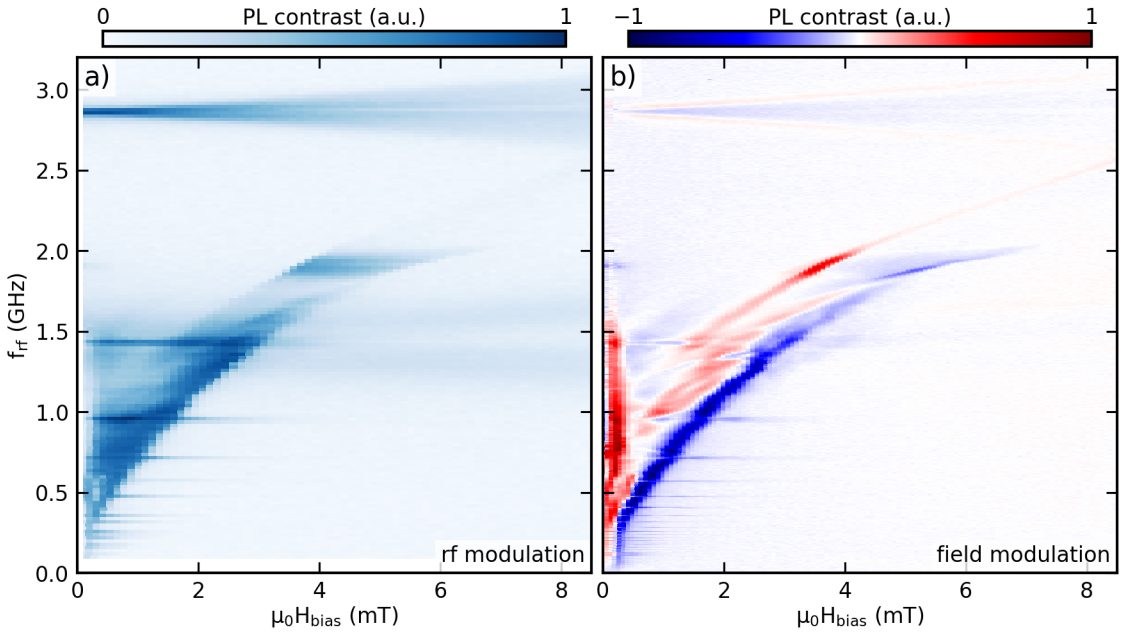

Fig. S3 | ODMR modulation techniques. Comparison of the two employed modulation techniques used to enable lock-in detection. a) Amplitude modulation of the rf excitation and b) modulation of the bias field. Both methods display the same features while b) can be understood as the derivative of a) with respect to bias field. Therefore, a change in PL signal is very pronounced and yields strong contrast in b), whereas plateaus visible in a) are not detected in b). This renders the two modulation methods complementary. The rf excitation power in both measurements is $19\,\mathrm{dBm}$.

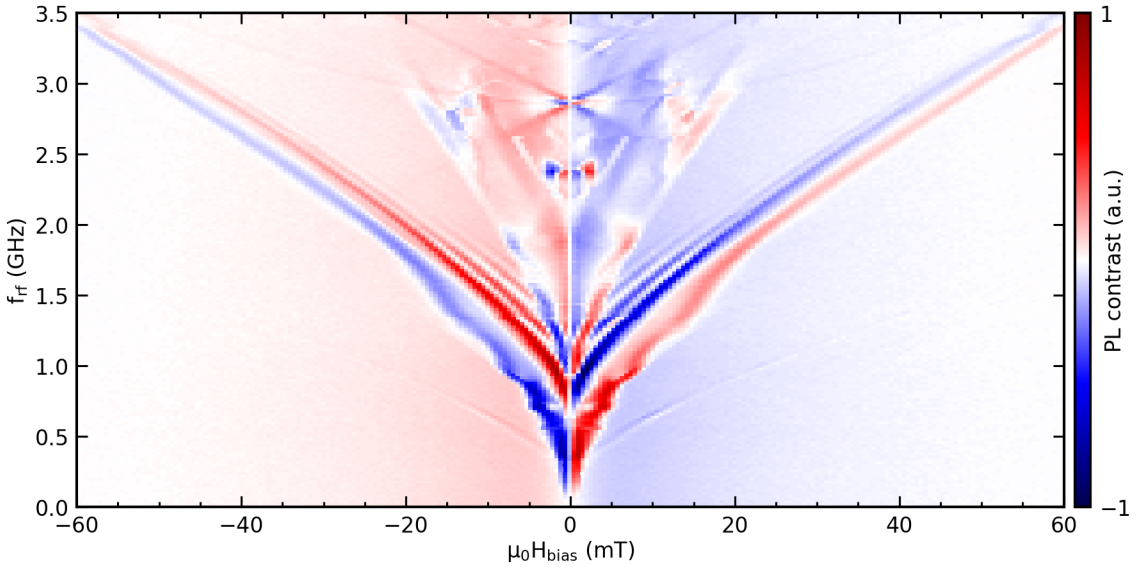

Fig. S4 | ODMR measurement of YIG. Analogous measurement on a $100\,\mathrm{nm}$-thick YIG film at $15\,\mathrm{dBm}$ excitation power. The low damping of YIG gives rise to plenty of spin wave modes which are experimentally accessible with the ODMR technique. However, the higher magnetic stiffness of YIG suppresses the generation of harmonics in the low-field regime observed in $Ni_{80}Fe_{20}$.

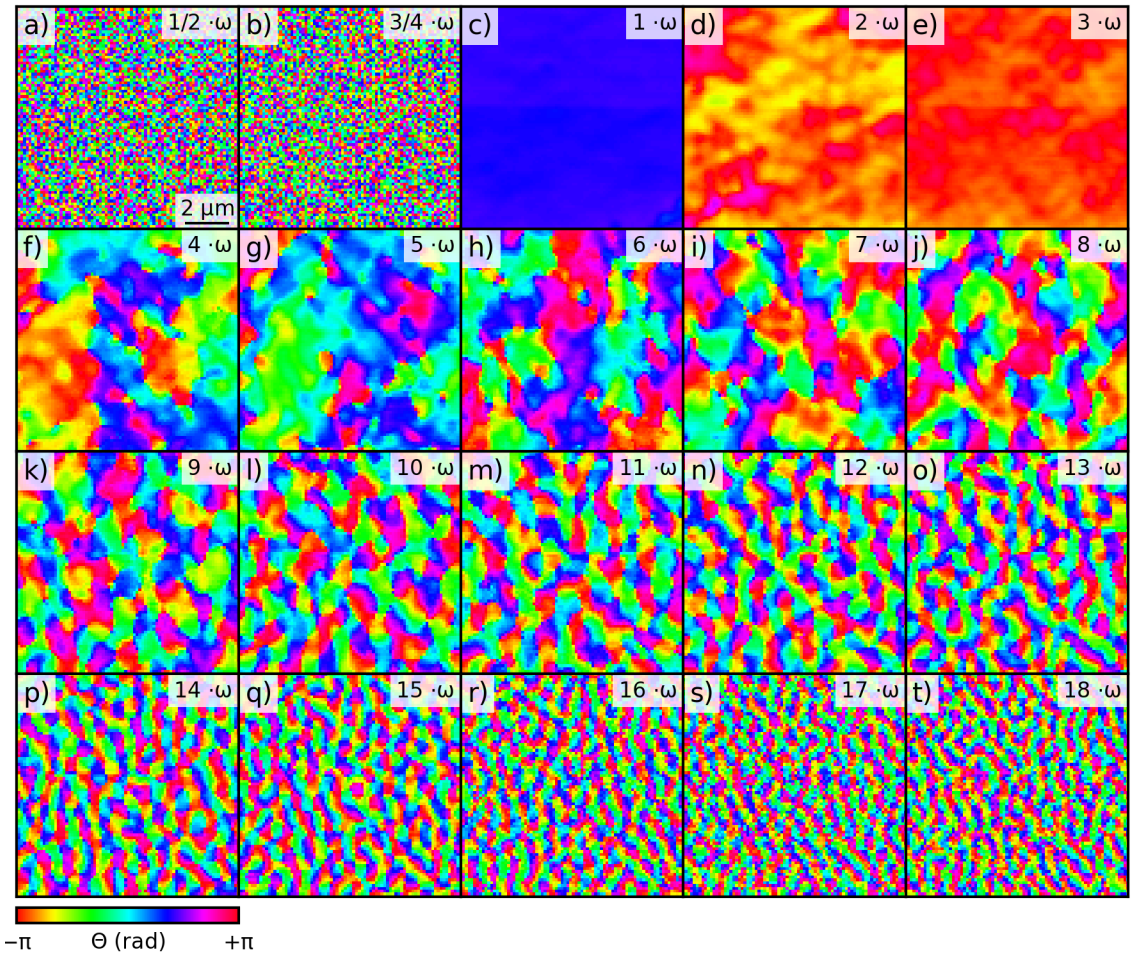

Fig. S5 | Spatially-resolved MOKE imaging of higher harmonics. SNS-MOKE measurements were performed with up to 20 different detection channels. Here, the phase of the dynamic response at the corresponding detection frequency is shown for $1/2\ \omega$ in a), $3/4\ \omega$ in b) and the 1^{st} - 18^{th} harmonic in panels c)-t), respectively. The excitation frequency was set to $159\,\mathrm{MHz}$ at a rf-power level of $19\,\mathrm{dBm}$ while the external magnetic field was fixed at $0.5\,\mathrm{mT}$. The non-integer harmonics show no signal but only random phase noise while for the integer harmonics this changes completely. For the first harmonics a mostly uniform phase is detected. However, for higher harmonic numbers the uniformity reduces and a phase stable spin wave pattern forms who's lateral dimensions decrease with frequency.

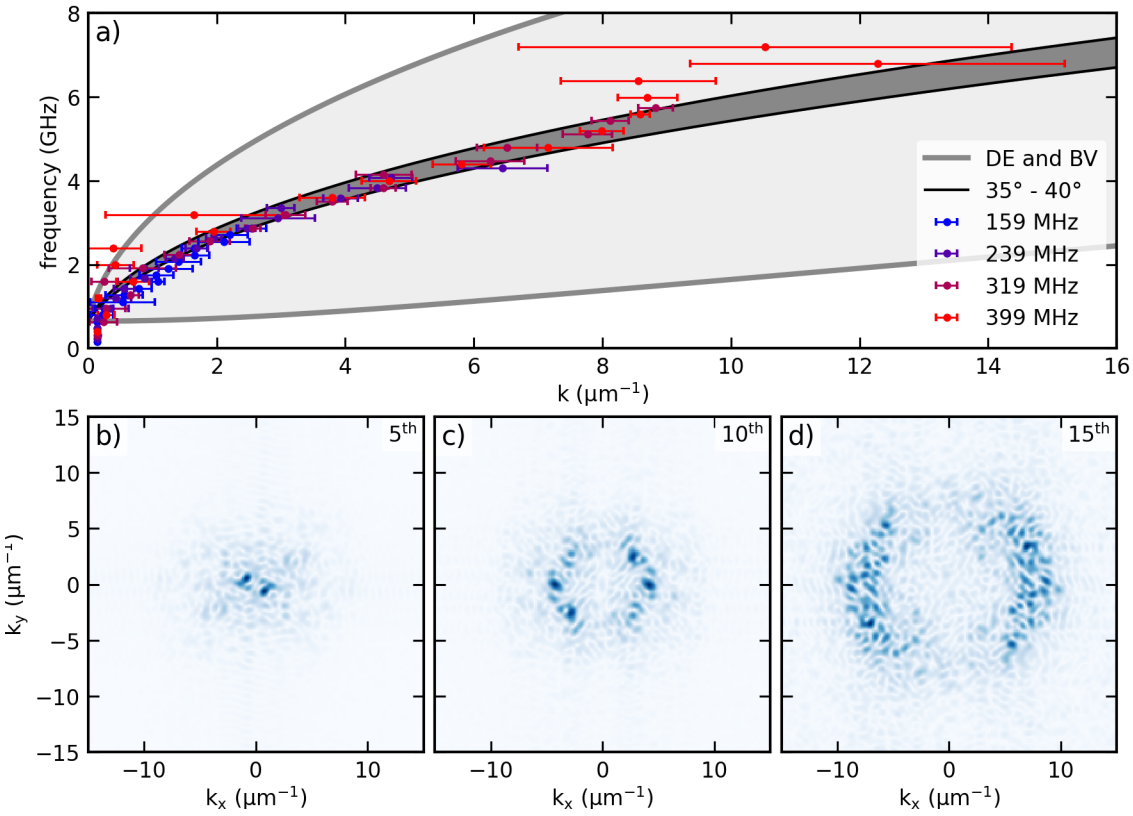

Fig. S6 | Wave vector spectrum for different excitation frequencies. In a) the in-plane wave number of higher harmonics extracted from spatially resolved phase maps at varying excitation frequencies is plotted. In addition, the spin wave dispersion branches in Damon Eshbach (DE) and backward volume (BV) geometry are depicted for an external magnetic field of $0.5\,\mathrm{mT}$ (grey lines). For harmonics at frequencies below the spin wave band a mostly uniform signal is detected resulting in $k = 0$. After passing the BV dispersion branch different wave vector components appear. Surprisingly, for harmonics at frequencies above $1\,\mathrm{GHz}$ the wave numbers follow a defined branch within the spin wave band which corresponds to angular orientations between $35°$ and $45°$ (dark grey). In panel b)-d) exemplary 2D-FFT patterns of the 5$^{\text{th}}$, 10$^{\text{th}}$ and 15$^{\text{th}}$ harmonics for an excitation frequency of $319\,\mathrm{MHz}$ again show the shift of the wave vector towards larger values with increasing harmonic mode number.

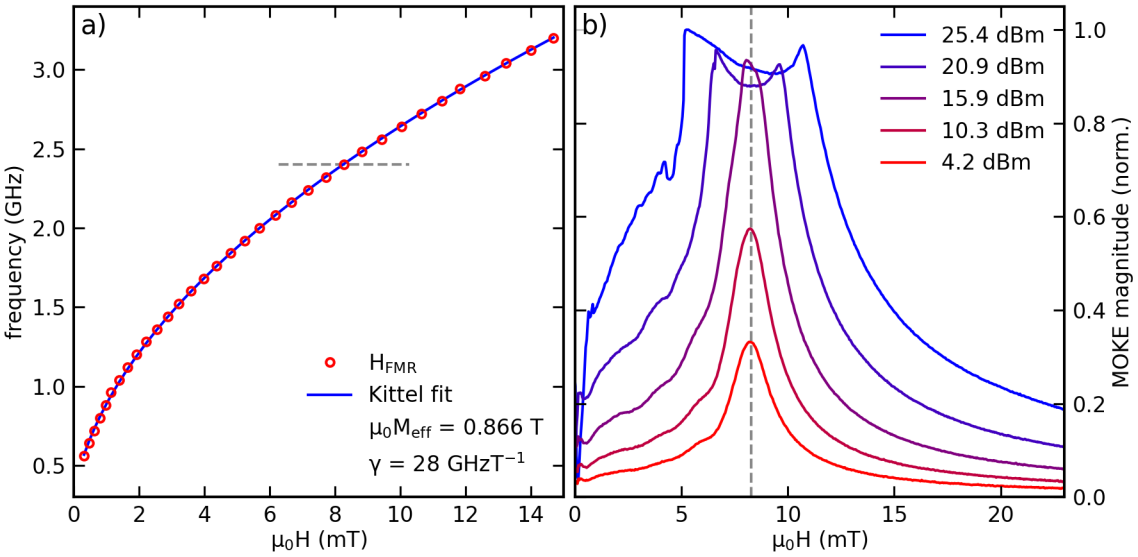

Fig. S7 | Optical FMR measurements and power dependent lineshape changes. a) Ferromagnetic resonance field extracted from frequency dependent SNS-MOKE measurements for low power excitation. The blue line shows a fit to the Kittel equation well matching the expected magnetic properties for $Ni_{80}Fe_{20}$. The dashed line indicates the region shown in b). Here, at a frequency of $2.4\,\mathrm{GHz}$ field swept measurements at different power levels were performed. The dashed line indicates the position of the low power FMR. For larger excitation levels the resonance broadens and shifts towards lower field values[14].